Bone microarchitecture characterization based on fractal analysis in spatial frequency domain imaging

Soraya Zehani,[a] Abdeldjalil Ouahabi,[b,c,*] Mourad Oussalah,[d] Malika Mimi,[e] Abdelmalik Taleb-Ahmed[f]

[a]University of Biskra, Faculty of Sciences and Technology, Electrical Engineering Department, Laboratory of LESIA, 07000 Biskra, Algeria.

[b]University of Tours, Polytech Tours, Electrical Engineering Department, Imaging and Brain INSERM U 930, 37200 Tours, France.

[c]University of Bouira, Computer Science Department, LIMPAF, 10000 Bouira, Algeria.

[d]Oulu University, Center for Ubiquitous Computing, Oulu, Finland.

[e]University of Mostaganem, Electrical Engineering Department, Laboratory of Signals and Systems, 27000 Mostaganem, Algeria,.

[f]IEMN DOAE UMR CNRS 8520, UPHF, 59313 Valenciennes, France.

Abstract

This paper suggests a new technique for trabecular bone characterization using fractal analysis of X-Ray and MRI texture images for osteoporosis diagnosis. Oste-oporosis is a chronic disease characterized by a decrease in bone density that can lead to fracture and disability. In essence, the proposed fractal model makes use of the differential box-counting method (DBCM) to estimate the fractal dimension (FD) after an appropriate image preprocessing stage that ensures a robust estimation process. In this study, we showed that within the frequency domain generated through discrete cosine transform (DCT), only a quarter of DCT coefficients are enough to characterize osteoporotic tissues. The algorithmic complexity of the developed approach is of the order of $\frac{N}{8}\log_2\frac{N}{8}$ where N stands for the size of the image, which, in turn, likely yields important gain in terms of medication cost. We report a successful separation of healthy and pathological cases in term of both P-value (using statistical Wilcoxon rank sum test) and margin difference. A comparative statistical analysis has been performed using a publicly available database that contains a set of MRI and X-Ray texture images of both healthy and osteoporotic bone tissues. The statistical results demonstrated the feasibility and accepted performance level of our fractal model-based diagnosis to discriminate healthy and unhealthy trabecular bone tissues. The developed approach has been implemented on a medical device prototype.

Keywords: Discrete cosine transform (DCT), Fractal Analysis, Fractal dimension (FD), Medical imaging, Osteoporosis, Trabecular bone texture.

1 Introduction

Osteoporosis is a common public health problem that weakens bones, which increases the risk of fracture, due to the porous trabecular microarchitecture (see Figure1). The disease has a significant impact on morbidity and mortality and poses serious health issues to more than 200 million people in the world according to the World Health Organization. In a clinical routine check-up, screening for osteoporosis is performed by measuring bone

*Address all correspondence to: Abdeldjalil Ouahabi, E-mail: ouahabi@univ-tours.fr

mineral density, which is a non-invasive procedure. However, trabecular microarchitecture cannot be evaluated without an invasive procedure.

Therefore, automatic methods that potentially characterize the trabecular bone texture using texture analysis are deemed very relevant[1]. For this purpose, texture analysis and classification have been widely used[2].

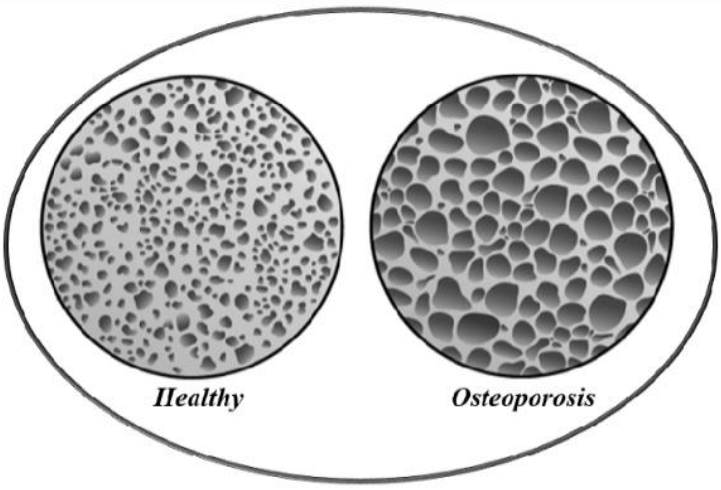

Fig. 1 Bone Microarchitecture: Healthy and Osteoporotic.

Besides, from an implementation perspective, several steps should be considered when carrying out any texture analysis technique. First, texture properties are described through a feature vector. The latter may involve either statistical features of image intensity domain or some structural representation that rather describes the spatial relationship of repetitive texture elements. Second, a classification task determines to which predefined class the given texture belongs to. Third, the whole image is partitioned into disjoint regions containing homogeneous textures[3]. Among the statistical-based features, one distinguishes the growing interest in fractal-like analysis[4-5], especially in medical applications. Indeed, the fractal theory, introduced by Mandelbrot[4], offers a nice framework for dealing with complex shapes and phenomena. It enables representing such shapes / phenomena by extending the classical concept of dimensionality of the systems to add a fractional index that corresponds to a measure of the space-filling nature of a rugged structure. This was also motivated by the observation that fractal dimension (*FD*) is relatively insensitive to image scaling and exhibits a strong correlation with human judgment of surface roughness[6] in the sense that the larger the value of *FD*, the rougher the appearance of the underlying fractal set. More specifically, a fractal is a geometrical object characterized by two fundamental properties: self-similarity and Hausdorff-Besicovich dimension[6]. Furthermore, a fractal generally exhibits irregular shapes that cannot simply be described by Euclidian dimension, but rather as an *FD* index. However, unlike the topological dimension, the *FD* index can take non-integer values, meaning that the way a fractal set fills its space is qualitatively and quantitatively different from how an ordinary geometrical set does. Because of its inherent and appealing properties, fractal and multifractal analyses are frequently used in biomedical signal and image processing[7-16].

Spatial and frequency domain approaches are two different techniques in image processing. In general, neighboring pixels within an image in the spatial domain tend to

be highly correlated. As such, it is desired to use an invertible transform to concentrate randomness into fewer decorrelated parameters. The discrete cosine transform (DCT) transforms a signal from a spatial (or time-domain, in the case of a 1D signal) domain into a frequency domain. Besides, DCT has been shown to be near-optimal for a large class of images in energy concentration and decorrelating[17]. Especially, DCT is widely applied in signal and image processing fields such as compression, classification and biomedical engineering[17-19] due to its excellent properties of grouping energy where the information is essentially carried out by the low-frequency coefficients.

Traditionally, the fractal dimension (*FD*) of an image is primarily estimated in the temporal and spatial domains. Indeed, the *FD* mostly quantifies the roughness or smoothness of time-series and spatial data in the limit as the observational scale becomes infinitesimally fine where the estimation is dependent on the availability of observations at sufficiently fine temporal or spatial resolution[20-22]. Methods developed for this purpose include box-counting (BC), differential box-counting method (DBCM)[23], Hall-Wood estimator, variogram estimator and its variants[24-25], level crossing[26]. The reader can consult, e.g., the review paper[27] and references therein for an in-depth comparison of these estimators. In contrast to time-series and spatial approaches, alternative methods rely on the frequency or spectral domain. In this context, the scaling law applies as the frequency growths to infinity, equivalent to the scale becoming infinitesimally small in the time domain. Examples of such approaches include the semi-periodogram estimator of Chan et al.[28]. The key advantage of handling the fractal dimension in the frequency domain is that many complex convolution operations in the spatial domain employed for correlation or filtering tasks can be simplified significantly in the frequency domain. Moreover, the anisotropic spatial distribution of a spectral energy density retains the spatial structure of a field[29]. Authors in[30] derived a discrete cosine transform-based fractal dimension using ordinary least square fit of periodogram parameters. In the same spirit, this paper advocates the use of DCT-based *FD* estimation for the purpose of bone texture characterization. The percentage of transformed image (DCT%) was employed to demonstrate the feasibility of the proposal using only a quarter of DCT coefficients. In the sequel, the approach highlights the importance of the preprocessing step as a pre-requisite for achieving acceptable results. In this respect, two variants of preprocessing stages have been investigated. The first one employs a median filter (MF) followed by a fractal analysis using DBCM. The second one uses a contrast enhancement (CE) followed by a DBCM. The developed approach is implemented on a medical device prototype that helps in osteoporosis diagnosis. By doing so, we expect to substantially reduce the associated medical costs and provide a valuable decision support system to clinicians in their attempt to diagnose osteoporosis disease.

This work extends our previous findings in[31] by including:

i) Two imaging modalities of trabecular bone textures: MRI and X-Ray images;

ii) Two preprocessing approaches based on median filter (MF) and contrast enhancement (CE);

iii) A directional analysis (anisotropy analysis) with several orientations from 0° to 360° with a step angle of 15° and quantifying the results with or without preprocessing stages.

Moreover, since the DCT has an excellent property of energy grouping: the information is essentially carried by the low-frequency coefficients, thereby, only a percentage of the total DCT coefficients were employed instead of all the DCT coefficients, in order to produce a robust fractal dimension in the DCT domain (DCT%).

Section 2 of this paper presents some of the related works. Materials and methods that include the overall methodology, which fruitfully combines image acquisition and database, data preprocessing, and discrete cosine transform in order to robustify the estimation of FD are described in Section 3. Section 4 exhibits the experimental results using images from a large database of trabecular bone texture whose results are compared, commented and discussed. Finally, the overall conclusion and perspective work are reported in Section 5. On the other hand, to ease the readability of the paper, we summarized in Table 1 the main acronyms employed throughout this paper.

Table 1 Main acronyms used in this paper.

Acronym	Description
ACC	Accuracy
AUC	Area under curve
ANN	Artificial neural networks
ap-WhE	Anisotropic piecewise Whittle estimator
BN	Bayes network
BTC	Bone texture characterization
CE	Contrast enhancement
DA	Degree of anisotropy
DBCM	Differential box-counting method
DCT	Discrete cosine transform
DCT%	Discrete cosine transform percentage (25%, 50%, 75% and 100%)
FD	Fractal dimension
fBm	Fractional Brownian motion
GLCM	Gray level co-occurrence matrix
H	Hurst coefficient (exponent)
H_{mean}	Mean Hurst coefficient (exponent)
HR-pQCT	High-resolution peripheral quantitative computed tomography
IVCM	Intravenous contrast medium
KNN	K-nearest neighbors
LBP	Local binary patterns
MRI	Magnetic resonance imaging
MSE	Mean square error
MF	Median filter
MDCT	Multi-detector computed tomography
MLP	Multilayer perceptron

NB	Naive Bayes
PSNR	Peak signal-to-noise ratio
ROI	Region of interest
RF	Random forest
SSIM	Structural similarity index metrics
SVM	Support vector machine
TNR	True negative rate
TPR	True positive rate
WC	Wrapped Cauchy
X-Ray	X-Ray images
σ	Standard deviation
Δ	Difference between the minimum and the maximum of the mean *FD* between each class (healthy and pathologic)

2 Related works

Relevant works on medical image processing based on the analysis and classification of trabecular texture are summarized in this section. Dougherty and Henebry[32] used the fractal signature and lacunarity for the measuring the texture of trabecular bone in clinical CT images. Harrar et al.[33] proposed a new method that involves a fractal model and Whittle estimator for Hurst exponent calculus, to asses bone microarchitecture and characterize trabecular bone radiographs. Zheng et al.[34] proposed a classification-based approach where the fractal dimension is among the set of feature attributes for discriminating healthy from osteoporotic subjects. The top performance is obtained by using the Bayes network classifier with an ACC of 79,3%. Oulhaj et al.[35] proposed a new approach based on wavelet phase decomposition and parametric circular model applied to classify trabecular textures from osteoporotic and healthy subjects using SVM and ANN classifiers. Singh et al.[36] investigated statistical features for different orders with and without preprocessing to classify osteoporotic trabecular bone form healthy cases using four classifiers: SVM, KNN, NB and ANN. The best result with an accuracy of 98% was achieved for the SVM classifier. Su et al.[37] proposed an encoded texture features to characterize bone textures based on two groups of new features, encoded GLCM (gray level co-occurrence matrix) and encoded LBP, each of which contains two subgroups. The first one results from encoding the Gabor and Hessian information into the GLCM features, while the second one employs LBP features and RF classifier. Harrar et al.[38] proposed an oriented fractal analysis method combining an anisotropic fractional Brownian motion model with an anisotropic piecewise white estimator to characterize trabecular bone radiograph. They validated their proposed approach using several well-known estimators on anisotropic and isotropic synthetic fractional Brownian motion images in different orientations in multiples of 45°. Houam et al.[39] proposed the combination of global and local information to better capture the image characteristics by

using a one-dimensional local binary pattern for bone texture classification. The aforementioned results support the hypothesis that 2D texture analysis can contribute to the identification of changes in trabecular bone microarchitecture. Similarly, the extensive work on image-based osteoporosis diagnosis has promoted several public databases to test and evaluate the performance of the developed approaches. Zou et al.[40] proposed the use of wavelet leader (WL) transformation to study trabecular bone patterns. After extracting WL from the trabecular texture, they used the two statistical texture characterization methods namely the gray level co-occurrence matrix (GLCM) and the Gray Level Run Length Matrix (GLRLM). Then they used two features, the energy from the GLCM and the Gray Level Non-Uniformity from the GLRLM to distinguish between the osteoporotic patients and control subjects and performed their method with ROC curves. Keni Zheng et al.[41] studied and developed mathematical methods and algorithms for disease diagnosis and tissue characterization of the trabecular bone texture using supervised learning techniques. They developed methods for the calculation of sparse representations to classify imaging patterns and explore the advantages of this technique over traditional texture-based classification. They evaluated the classification performances of their methods using a 30-fold cross-validation. Table 2 summarizes some of the key works in this field in recent years (2016-2019).

Table 2 Comparison of some of main studies for trabecular bone texture characterization.

Reference	**Database**	**Site**	**Methodology**	**Features (or their number)**	**Performance measure**	**ACC, AUC, p**	**Year**
M. R. K. Mookiah *et al*.[42]	MDCT Data images (trabecular bone from HR-pQCT) with and without IVCM.	Vertebral	Texture analysis using GLCM (energy, entropy, homogeneity, …). Classifiers : SVM	8	Correlation r $p-value$ ACC	r up to 0.96 $p < 0.0001$ ACC= 83%	**2018**
Zheng and Makrogiannis[34]	BTC challenge data, healthy/osteoporosis bone radiograph.	Calcaneus	Correlation-based features selection. Classifiers: NB, MLP, BN and RF.	723 123 (Selected)	TPR, TNR, ACC and AUC.	ACC: 79,3%, AUC: 81%	**2016**
A. Singh *et al*.[36]	Patients with osteoporosis fractures of hip or vertebral or wrist/Control patients. 2004-2006, Orleans Hospital (France). X-Ray images.	Calcaneus	First and second order statistics features with and without preprocessing. Classifiers: SVM, NB, KNN and ANN.	6	ACC	Without preproc.<70%. With preproc. > 95%. The best ACC is obtained for SVM: 97,87%	**2017**
H. Oulhaj *et al*.[35]	2014 Challenge IEEE-ISBI : Bone Texture Characterization (X-Ray modality)	Calcaneus	Wavelet decomposition and circular parametric models. Classifiers : SVM and ANN.	WC and Gabor filters: 48 Fractal: H_{mean} GLCM: 64 LBP: 128	ACC, ROC, AUC and $p-value$.	The best result achieved with WC and Gabor models. SVM : 95,98%	**2017**

K. Harrar et al.[38]	Trabecular texture (X-Ray modality)	Calcaneus	Oriented fractal analysis using estimators (ap-fBm, ap-WhE) for different orientations.	$H_{mean} \pm \sigma$	$p - value$	$p < 2.36 \times 10^{-10}$	**2018**
R. Su *et al.*[37]	2014 Challenge IEEE-ISBI : Bone Texture Characterization (X-Ray modality)	Calcaneus	Encoded GLCM and encoded LBP features. Gabor and Hessian information used. RF Classifier.	Raw: 80 GLCM: 96 LBP: 384	ACC	The best results achieved with LBP: 60.8%. and with features selection: 71.2%	**2018**
Keni Zheng *et al.* [41]	TCB challenge dataset.	Calcaneus	Ensemble of sparse classifiers using 30-fold cross-validation.	FD, LBP, Gabor filter, DWT, DCT, FFT, edge histogram, Law's energy masks for 723 features.	ACC AUC	ACC = 70,7% AUC = 74,4%	**2019**

3 Materials and Methods

3.1 *Motivation*

Strictly speaking, the aforementioned works of fractal methods for texture classification reinforces the earlier work of Mandelbrot and Van Ness[43], among others, which showed that FD conducted alone performs moderately and was often outperformed by many other standard approaches as concluded by Du Buf et al.[44.] Instead of augmenting the dimension of feature space, an alternative approach consists in transforming the original image into a transformed image whose FD value becomes more reliable in the view of the context under consideration. In this respect, one shall mention the work of Chaudhuri and Sarkar[45] where the transformation is meant to capture the coarseness and directionality, yielding a high (low) gray-valued image and horizontally (vertically) smoothed image. In the same spirit, the idea pursued in this paper is to investigate the use of DCT transformation to enhance the efficiency of the fractal dimension such that the bone texture classification-based diagnosis of medical images is enhanced. Indeed, there is often a high correlation between neighboring pixels in the spatial domain, which generates redundancy in the information. As such, it is desired to use an invertible transform to concentrate randomness into fewer decorrelated parameters. For this purpose, the use of discrete cosine transform (DCT) is shown to be particularly useful[17-19, 46-48] where the key information is essentially carried out by the low-frequency coefficients. Therefore, there is an implicit evidence that the DCT could contribute to capturing the coarseness and the directionality, which, in turn, makes the estimation of the FD more robust. Some preliminary results in this direction have been reported in[31].

The process is also ultimately related to the *FD* estimation algorithms employed. One distinguishes the popularity of box-counting (BC) and differential box-counting method (DBCM)[27], which uses the spatial domain and without necessarily requiring extensive preprocessing stages.

More specifically, this paper introduces a combination scheme of a fractal with DCT for the bone texture characterization and uses the percentage of transformed image

(DCT%) for the estimation of the fractal dimension in the frequency space. Also, the influence of the preprocessing stage is quantified using either the median filter (MF) or the contrast enhancement (CE) approach. Besides, we investigated the directional analysis (anisotropy analysis) by varying the orientation from 0° to 360° with a step angle of 15°. This is performed both without preprocessing phase and with a preprocessing phase in the spatial domain and DCT domain. Finally, the newly established algorithms are tested on our database that contains a set of MRI and X-Ray images with texture ROIs of trabecular bone tissues corresponding to both healthy and osteoporosis cases[49-50].

3.2 *Image acquisition and database*

Patients were selected from the department of Rheumatology of the University Hospital of Lille to build a local database. This database contains a set of trabecular bone texture of X-Ray images and MRI in the grey level extracted from 100 patients.

The database was generated using ElitePlusTM for X-Ray images with the following settings: 1-mm slice thickness, field view = 140 mm, matrix size = 512×512 pixels and a maximum spatial resolution of approximately 400 μm. For each patient, four consecutive axial and four consecutive coronal slices of the nondominant forearm were selected. While for MR-images, the database was generated using Siemens Magnetom Open of 1.5 Tesla. The characteristics of the MRIs are as follows: field view = 360 mm, spatial resolution = 512×512 pixels, 12 lateral cut planes with a 4 mm inter-slice distance, cutting thickness = 4 mm, side of each pixel = 0.7031 mm and the parameters for measuring the T1 weighted acquisition sequence are: $T_R = 851\ ms$, $T_E = 30\ ms$.
The choice of ROIs is such that its shape is squared with a relatively large radius to cover the key milestones that may be observed in the image. These are extracted from the trabecular part (see Figure 2) of patients whose mean age before menopause is 35±10 years and postmenopausal women with a mean age of 64 ± 10 years. The database includes both healthy and osteoporosis cases with various sizes, which are all coded using 8-bit numbers. Figure 3 shows an example pertaining to both healthy and osteoporosis cases for MRI and X-Ray images. From this figure, we note the difference in the structure and the contrast between these two imaging modalities. For instance, the bony structure in X-Ray images has a high contrast compared to that of MRI that has a low contrast.

Fig. 2 Axial slices of radius and selection of Region of Interest (ROI).

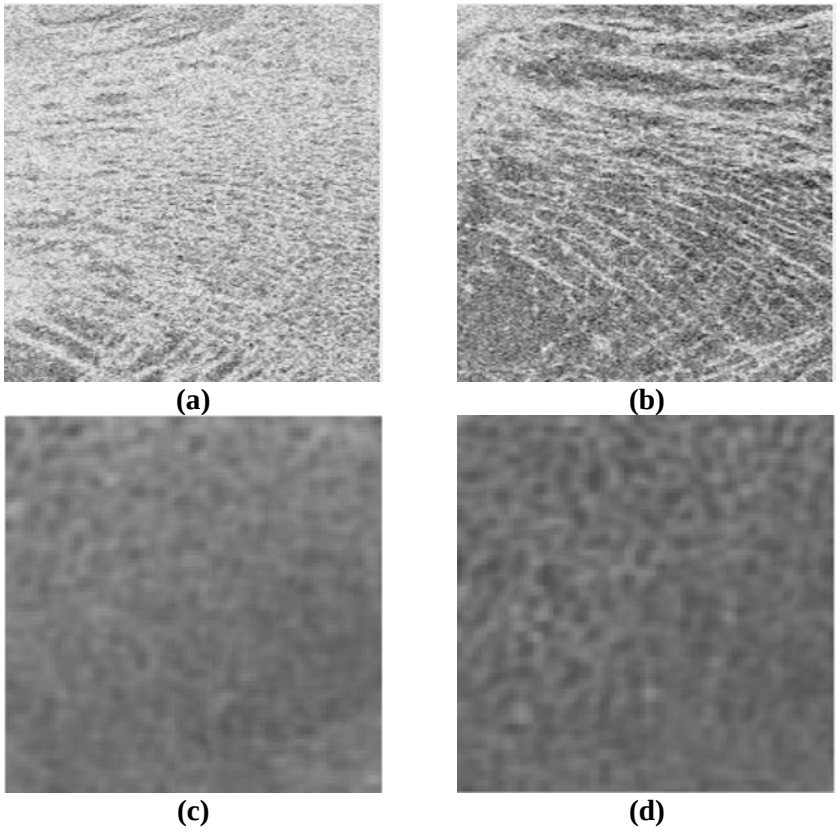

Fig. 3 Extracted healthy and pathological ROIs: (a): Healthy MRI, (b): Osteoporosis MRI, (c): Healthy X-Ray image and (d): Osteoporosis X-Ray image.

3.3 Data preprocessing

Two types of preprocessing techniques were considered. The first one involves the use of a standard median filter (MF) to the raw image to filter out possible noise occurrence, which also helps subsequent image processing stages. Median filters are useful in reducing random noise. The median filtering process is accomplished by sliding a window over the image. The second one involves the use of image contrast enhancement (CE). The aim of the image enhancement is to improve the perception of information in images, e.g., to improve the characteristics or quality of the initial image. For this purpose, histogram equalization is mainly used to enhance the contrast of the images. On the other hand, Gamma correction is used to control the level of contrast enhancement or to correct image's luminance. The latter addresses the problem of improving the visibility of significant features and the quality of the underlying medical image. This also allows us to reduce the image's noise and ultimately, to increase the contrast of the structures of interest, which, in turn, facilitates the diagnosis process. A typical and a simple contrast enhancement consists of adjusting the image intensity values such that 1% of data is saturated at low and high intensities of the original image through a linear or non-linear stretching so that the lowest image intensity is mapped to the bottom and the highest to the top. Whereas the bottom and top covers 99% of the intensity ranges in the underlying color space model. This approach is now part of textbook material and implemented in most image processing toolboxes (see, e.g, https://www.mathworks.com/products/image.html). Therefore, because of its simplicity and availability this contrast enhancement approach is employed throughout our subsequent methodology.

It should be noted that the Lille University Hospital database of subsection 3.2 contains some X-Ray and MRI images that are by nature slightly noisy as well, nevertheless, for the sake of robustness analysis and to quantify the noise influence, we also created noisy images. The latter were obtained by injecting an additive zero mean random noise with a variance of 0.01 to the raw X-Ray and MRI images yielding a set of noisy MRI and noisy X-Ray images that will be tested in subsequent reasoning, See for example, Fig.4e and Fig.4j for instances of noisy MRI image and noisy X-Ray image, respectively.

On the other hand, the application of such preprocessing stage in terms of filtering and contrast enhancement expects to positively impact the performance of the discrimination power of the developed algorithm (s), especially for noisy images.

Figure 4 shows the two imaging modalities (MRI in the first row and X-Ray images in the second row) from our database when the images are preprocessed using either MF or CE methods.

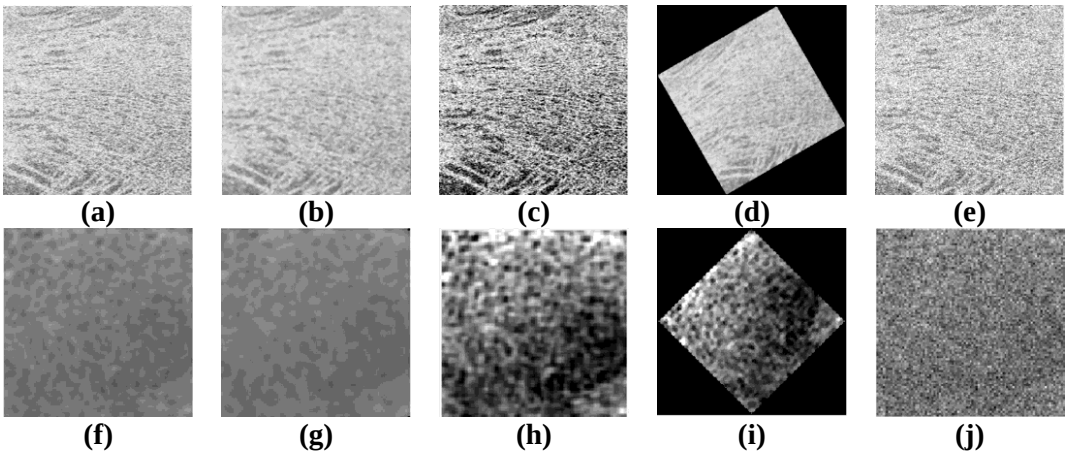

Fig. 4 Two samples of bone MRI (first row) and X-Ray images (second row) textures of healthy subjects: (a) and (f): Original input textures; (b) and (g): Preprocessed with the median filter (MF); (c) and (h): Preprocessed with the contrast enhancement (CE); (d): Preprocessed MRI with (MF) and rotated 30°, (i): Preprocessed X-Ray images with (CE) and rotated 45°, (e): Noisy MRI, (j): Noisy X-Ray images.

3.4 Discrete cosine transform (DCT)

The principal advantage of DCT is the removal of redundancy between neighboring pixels, yielding uncorrelated transform coefficients that can be encoded separately. Particularly, DCT exhibits an excellent energy compactness for highly correlated images, which allows the DCT to pack input data into as few coefficients as possible. This raises the problem of how to reduce the coefficients exhibited by the DCT. It is, for instance, acknowledged, see[14], that DCT coefficients are divided into low, middle and high frequencies, where low-frequency components are rather correlated with illumination condition while high-frequency coefficients are more associated to noise and small variations. Middle frequency components often contain useful information about the structure of the image. Several studies tackled the problem of the appropriate selection of DCT components. Commonly employed is the first percentage; namely, DCT ($M\%$) of an ($N \times N$) image would retain the first ($N \times N \times M\%$) coefficients. Alternative approaches make use of complex minimization criteria. For instance, Pan et al.[47] proposed to select coefficients that minimize the reconstruction error. Choi et al.[19] proposed to use energy probability to generate a frequency mask. Sanderson and Paliwal[48] used a polynomial coefficient derived from the 2D-DCT coefficients of neighboring blocks.

In the context of image reconstruction, it was reported, for instance, that DCT (25%) introduces a blurring effect on all images, while DCT (50%) provides acceptable reconstruction capabilities, and DCT (75%) yields excellent reconstruction of all images. Therefore, it is interesting to investigate the effect of DCT ($M\%$) on image fractal analysis. Figure 5 summarizes the distribution of the DCT coefficients for ($N \times N$) image.

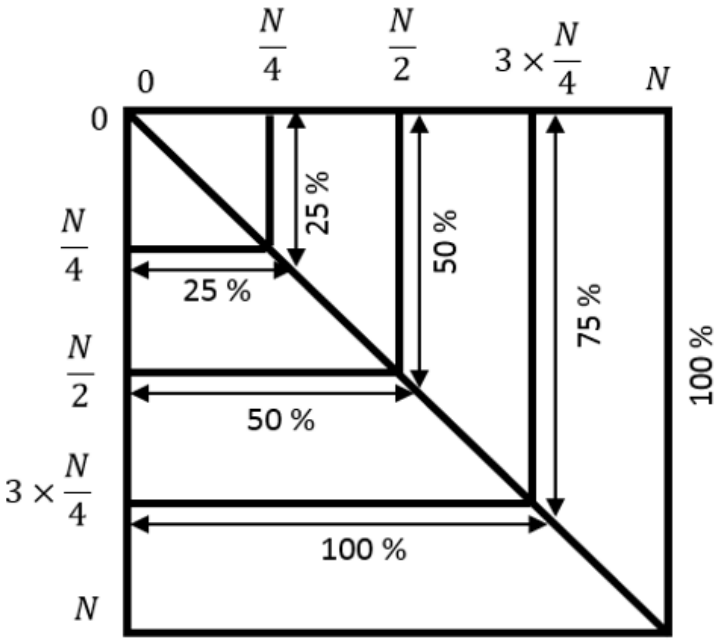

Fig. 5 Distribution of DCT% coefficients for an $(N \times N)$ image.

3.5 *Proposed algorithm*

A generic description of the algorithm for trabecular texture analysis to estimate the *FD* value using a combination of image processing and DCT transform is summarized in Algorithm 1 shown in Table 3.

Table 3 Pseudo-code for *FD* estimation with DCT.

Algorithm 1: *Estimation of FD with DCT.*

Input : Texture.

Output : *FD* value.

1. Apply a preprocessing stage (median filter (MF) or contrast enhancement (CE)) to the texture.
2. Apply DCT to the filtered and output DCT coefficients for DCT25%, DCT50%, DCT75% and DCT100%.

FOR each DCT % **Do**
  FOR each size of Box **Do**
    3. Apply DBCM to filtered texture to estimate the *FD* value.
  END

END

Besides, for the directional analysis of trabecular textures, a generic description of the algorithm for obtaining the directional *FD* values using a combination of image processing and DCT transform is summarized in Algorithm 2 highlighted in Table 4.

Table 4 Estimation of directional *FD* with DCT

Algorithm 2 : *Estimation of directional FD with DCT.*

Input : Texture.

Output : Directional *FD* values : $DF(\theta)$.

FOR each texture **do**

1. Apply a preprocessing stage (median filter (MF) or contrast enhancement (CE)) to the texture.
2. Rotate the preprocessed texture by angle θ: $(\theta = 0°:15°:360°)$.

FOR each preprocessed and rotated $ROI\ (\theta)$, **do**

3. Apply the DCT to the $ROI\ (\theta)$.
4. Apply the DBCM to the DCT to estimate the *FD* value: $DF(\theta)$.

END

END

4 Results and discussion

4.1 Setup and performance metrics

Throughout our experiment, one distinguishes between MRI and X-Ray images where separate results will be presented. In both cases, one also distinguishes between healthy and osteoporosis cases. To evaluate the ability of the fractal dimension to discriminate between healthy and osteoporosis cases, the statistical Wilcoxon rank-sum test, which can be applied to unknown distributions, was employed. This evaluates the following hypothesis H_0 against H_1:

H_0: FDs of Healthy and Osteoporosis Images have the same median

H_1: FDs of Healthy and Osteoporosis Images have distinct medians *(H_0 not valid)*

Especially, at the default 5% significance level, a $p-value$ for the above test of less than 0.05 ($p \leq 0.05$) indicates the rejection of the null hypothesis, and therefore, the ability of the *FD* estimate to discriminate healthy from osteoporosis cases. On the other hand, a $p-value$ (strictly) greater than 0.05 ($p > 0.05$) is equivalent to a failure of the *FD*-based approach to discriminate the healthy tissue from osteoporosis tissue.

In addition to the statistical test, we also present the results in terms of the minimum, maximum, mean and standard deviation ($m \pm \sigma$) of the *FD* values for each class of images. On the other hand, for the ease of comparison, we evaluated the maximum difference between the *FD* estimation in osteoporosis (FD_P) and healthy (FD_H) cases, which distinguishes the existence or absence of overlap between the two estimates. More specifically, this can be quantified as:

$$\Delta = \begin{cases} \min(FD_P) - \max(FD_H) & if \quad FD_P > FD_H \\ \min(FD_H) - \max(FD_P) & if \quad FD_H > FD_P \end{cases} \tag{1}$$

Especially, a negative value of Δ translates to a likely overlapping between the *FD* estimates, or, equivalently, a failure of the *FD* estimation-based approach to distinguish

healthy patterns from osteoporosis patterns. While a positive Δ corresponds to a successful operation.

Besides, in order to evaluate the impact of the preprocessing stage, the results with and without preprocessing are also presented and commented accordingly.

4.2 *Estimation of FD without preprocessing*

Table 5 and Table 6 summarize the statistical analysis of the *FD* using DBCM applied to the MRI and X-Ray images, respectively. On the other hand, given the already pointed sensitivity of the DBCM approach to the size of the boxes, and in the light of the previous work, see, e.g.,[31,49-51] where a linearly increasing box size for DBCM has been advocated, we compared the outcome of three linearly increasing box sizes (which roughly rounds up and down the minimum box size given the image pixel resolution). This yields sizes of ε ranging from 5 to 30 pixels, 5 to 35 pixels, and, finally, from 5 to 40 pixels, all by a step of 5 as in[31].

Table 5 Statistical analysis of *FD* using DBCM without preprocessing for MRI.

Box size		[5: 5: 30]	[5: 5: 35]	[5: 5: 40]
Healthy	$m \pm \sigma$	2.6930±0.1172	2.4555±0.1034	2.2319±0.1269
	max	2.8268	2.5715	2.3795
	min	2.6045	2.3669	2.1240
Osteoporosis	$m \pm \sigma$	2.6262±0.1094	2.3802±0.1022	2.1650±0.1153
	max	2.7417	2.4909	2.2938
	min	2.5262	2.2627	2.0645
Δ		-0.1372	-0.144	-0.1653
$p-value$		0.0706	0.0708	0.0708

Table 6 Statistical analysis of *FD* using DBCM without preprocessing for X-Ray images.

Box size		[5: 5: 30]	[5: 5: 35]	[5: 5: 40]
Healthy	$m \pm \sigma$	1.9832±0.1314	1.7506±0.1388	1.5482±0.1257
	max	2.1252	1.8844	1.7158
	min	1.8718	1.6279	1.4350
Osteoporosis	$m \pm \sigma$	2.0999±0.1136	1.8524±0.1268	1.6669±0.1130
	max	2.2376	1.9902	1.7930
	min	2.0013	1.7377	1.5667
Δ		-0.1239	-0.1467	-0.1491
$p-value$		0.0711	0.0711	0.0703

The results highlighted in Table 5 and Table 6 demonstrate the following:

1) The complexity of the DBCM implementation increases with the box size. In this respect, the case of box size [5 30] reveals the lowest computational cost. Besides, the whole implementation is performed in Matlab platform, which allows us to benefit from the highly cost-effective image processing subroutines.
2) In the case of a linear increase of box size in DBCM, the *FD* estimates decrease with the size of the box.
3) The values of Δ and $p-value$ parameters ($\Delta < 0$ and $p > 0.05$) indicate the *FD*-based approach cannot distinguish the healthy from osteoporosis cases when no preprocessing stage was employed.
4) The comparison of the various box sizes in the DBCM implementation indicates a

marginally close performance of the linearly increasing box size [5 30], [5 35] and [5 40]. This is partly explained by the nature of employed images where the presence of a (curve) line with distinct thickness influences the *FD* estimate negatively when the box sizes are not uniform. Such a phenomenon has also been noticed in related studies, see, e.g.,[52].

5) On the other hand, the statistically insignificant variation of the outcomes of the three linearly varied box sizes and the absence of further theoretical investigation motivate us to restrict to only a single box size choice; namely, [5 30] with a step size of 5 pixels.

6) The comparison between MRI and X-Ray images reveals that the *FD* estimation fails to distinguish the healthy from the osteoporotic tissues in both cases. On the other hand, scrutinizing the Δ value indicates a greater uncertainty/confusion associated with MRI images.

4.3 *Estimation of FD with preprocessing*

Two variants of preprocessing stages have been used independently for both MRI and X-Ray images; namely the standard MF, consisting of a mask of (3×3) pixels, and the CE. The latter is obtained by the adjustment of the image intensity values such that 1% of data is saturated at low and high intensities, which, sometimes, substantially increases the quality of the raw image. Figures (6-7) present the performance metrics in terms of *PSNR* and *SSIM*[53] for MRI and X-Ray texture images of both healthy and osteoporosis cases when the preprocessing stage is through the median filter and contrast enhancement methods.

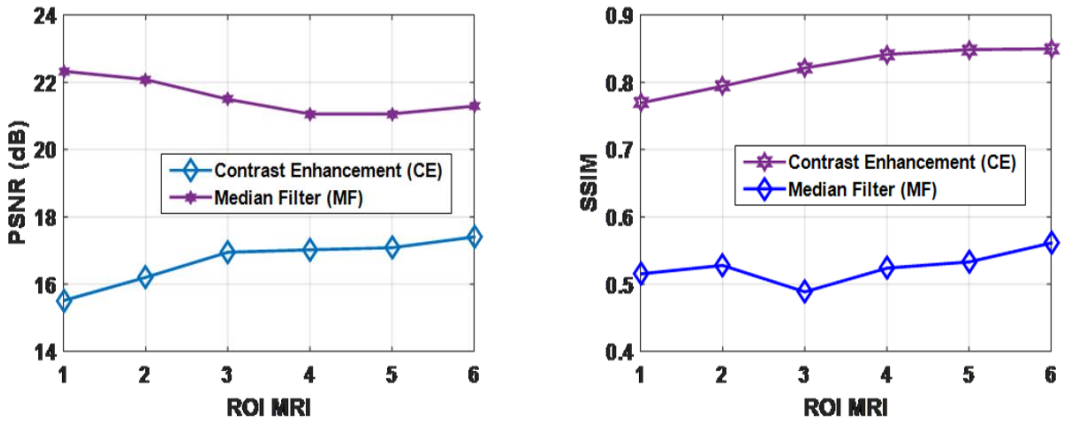

Fig. 6 Performance evaluation of contrast enhancement (CE) versus median filter (MF) in terms of objective metrics (peak signal-to-noise ratio (*PSNR*) and structural similarity index (*SSIM*)) for MRI.

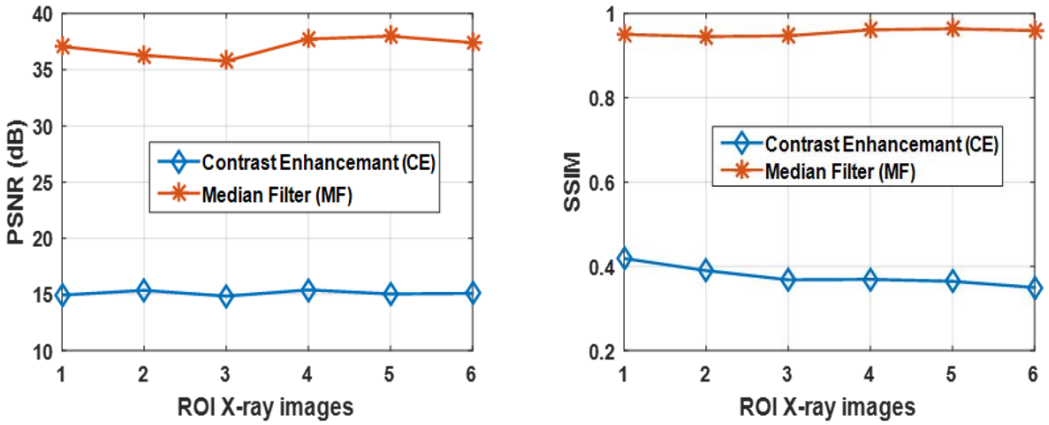

Fig. 7 Performance evaluation of contrast enhancement (CE) versus median filter (MF) in terms of objective metrics (peak signal-to-noise ratio (*PSNR*) and structural similarity index (*SSIM*)) for X-Ray images.

After the preprocessing stage, the DCT transform of the filtered image (using DCT 25%, DCT 50%, DCT 75%, and DCT 100%) has been performed and its associated *FD* using DBCM of box size [5 30] is calculated accordingly. The results for both MRI and X-Ray images are summarized in Tables 7-10. Similar to the previous section, the results are presented in terms of mean, standard deviation, maximum, minimum, Δ, and the $p-value$ for 300-selected MRI and 300-selected X-Ray images including both healthy and osteoporosis cases, corresponding to 150 ROI trabecular textures for each group (healthy and pathological) and each modality (MRI and X-Ray images).

Table 7 Statistical analysis of *FD* using median filter (MF) + DCT%+DBCM for MRI.

Box size [5: 5: 30]	*FD*	Without DCT	DCT25%	DCT50%	DCT75%	DCT100%	DCT25% (Noisy images)
	$m \pm \sigma$	2.7407±0.0864	2.6860±0.0302	2.6807±0.0298	2.6777±0.0305	2.6753±0.0336	2.6512±0.0345
Healthy	max	2.8467	2.7427	2.7409	2.7395	2.7372	2.6921
	min	2.6475	2.6433	2.6425	2.6400	2.6383	2.6275
	$m \pm \sigma$	2.6390±0.0817	2.5942±0.0267	2.5914±0271	2.5940±0.0206	2.5974±0.0143	2.5728±0.0342
Osteoporosis	max	2.7252	2.6367	2.6349	2.6306	2.6279	2.6245
	min	2.6139	2.5499	2.5513	2.5622	2.5837	2.5291
Δ		-0.0777	0.0066	0.0076	0.0094	0.0104	0.0030
$p-value$		0.0602	1.4045e-04	1.4045e-04	1.4045e-04	1.4045e-04	1. 4045e -04

Table 8 Statistical analysis of *FD* using contrast enhancement (CE) + DCT%+DBCM for MRI.

Box size [5: 5: 30]	*FD*	Without DCT	DCT25%	DCT50%	DCT75%	DCT100%	DCT25% (Noisy images)
	$m \pm \sigma$	2.6334±0.0649	2.6363±0.0231	2.6391±0.0232	2.6414±0.0233	2.6484±0.0230	2.6205±0.0305
Healthy	max	2.7410	2.6876	2.6876	2.6862	2.6977	2.6985
	min	2.5643	2.5875	2.5869	2.5894	2.5923	2.5828
	$m \pm \sigma$	2.5398±0.0576	2.5542±0.0218	2.5471±0.0219	2.5471±0.0220	2.5537±0.0218	2.5362±0.0300
Osteoporosis	max	2.6064	2.5821	2.5809	2.5787	2.5819	2.5793
	min	2.4911	2.5242	2.5246	2.5225	2.5211	2.5162
Δ		-0.0421	0.0054	0.0060	0.0107	0.0104	0.0035
$p-value$		0.0511	1.4045e-04	1.4045e-04	1.4045e-04	1.4045e-04	1.4756e-04

Table 9 Statistical analysis of *FD* using median filter (MF) + DCT%+DBCM for X-Ray images.

Box size **[5: 5: 30]**	*FD*	Without DCT	DCT 25%	DCT50%	DCT75%	DCT100%	DCT25% (Noisy images)
Healthy	$m \pm \sigma$	1.9983±0.0887	2.2444±0.0095	2.2449±0.0100	2.2413±0.0126	2.2439±0.0117	2.2468± 0.0204
	max	2.0629	2.2651	2.2603	2.2556	2.2639	2.2714
	min	1.9069	2.2435	2.2332	2.2213	2.2298	2.2381
Osteoporosis	$m \pm \sigma$	2.1531±0.0823	2.2768±0.0088	2.2771±0.0091	2.2738±0.0097	2.2760±0.0072	2.2794± 0.0110
	max	2.1376	2.2979	2.2922	2.2903	2.2865	2.3015
	min	2.0323	2.2610	2.2642	2.2581	2.2674	2.2737
Δ		-0.0306	0.0041	0.0039	0.0025	0.0035	0.0023
$p - value$		0.0615	1.5589e-04	1.5589e-04	1.5589e-04	1.5589e-04	1. 5589e -3

Table 10 Statistical analysis of *FD* using contrast enhancement (CE) + DCT%+DBCM for X-Ray images.

Box size **[5: 5: 30]**	*FD*	Without DCT	DCT25%	DCT50%	DCT75%	DCT100%	DCT25% (Noisy images)
Healthy	$m \pm \sigma$	1.9381±0.0795	2.2042±0.0261	2.2046±0.0263	2.2049±0.0262	2.2053±0.0260	2.2328± 0.0314
	max	2.0205	2.2506	2.2049	2.2025	2.2018	2.2712
	min	1.8542	2.1695	2.1284	2.1283	2.1283	2.1924
Osteoporosis	$m \pm \sigma$	2.1153±0.0647	2.2851±0.0297	2.2856±0.0298	2.2861±0.0296	2.2844±0.0295	2.3024± 0.0340
	max	2.1658	2.3378	2.2965	2.2968	2.2974	2.3484
	min	2.0532	2.2587	2.2131	2.2093	2.2088	2.2764
Δ		-0.0327	0.0081	0.0082	0.0068	0.0070	0.0052
$p - value$		0.0556	1.5540e-04	1.5540e-04	1.5540e-04	1.5540e-04	1.6154e-3

Especially, a quick look at the results highlighted in Tables 7-10 reveals both the importance of the DCT task and the sufficiency of a small proportion of DCT components (25 % for both MRI and X-Ray images) to achieve a successful discrimination of healthy from osteoporosis cases. Besides, a fair comparison between MF and CE preprocessing indicates a marginal outperformance of median (resp. CE) like-approach in the case of MR images (resp. X-Ray images) as revealed by the value of the Δ entity. This provides further motivation grounds for subsequent analysis of the image database. On the other hand, instead of displaying global results across all images highlighted in Tables 7-10, through averaging operation, it is also interesting to see the variations of the *FD* across individual images that highlight key patterns. For this purpose, Figure 8 and 9 provide an example of *FD* estimate for both healthy and osteoporosis cases of images pertaining to the same contextual scenario (described in the database by letters) G, S, O, B and T for healthy and C, U, K, M, E for osteoporosis in case of MRI. In the context of X-Ray images P, A, R, I and Z for healthy and V, X, F, N, and W for osteoporosis bones. For illustration purposes, we deliberately restricted to the image classes exhibiting important visual variations. In terms of pre-processing tasks, we deliberately restricted to median filter (MF) for MRI images and CE for X-Ray images because of the results pointed out in Tables 7-10. The lines in blue represent the healthy case and the lines in red represent the osteoporosis case.

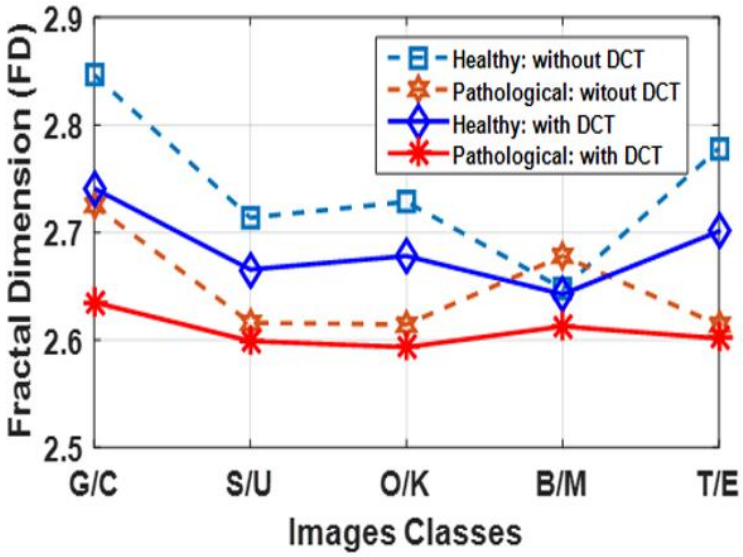

Fig. 8 Variation of the *FD* preprocessed using MF with DCT 50% and without DCT for MRI.

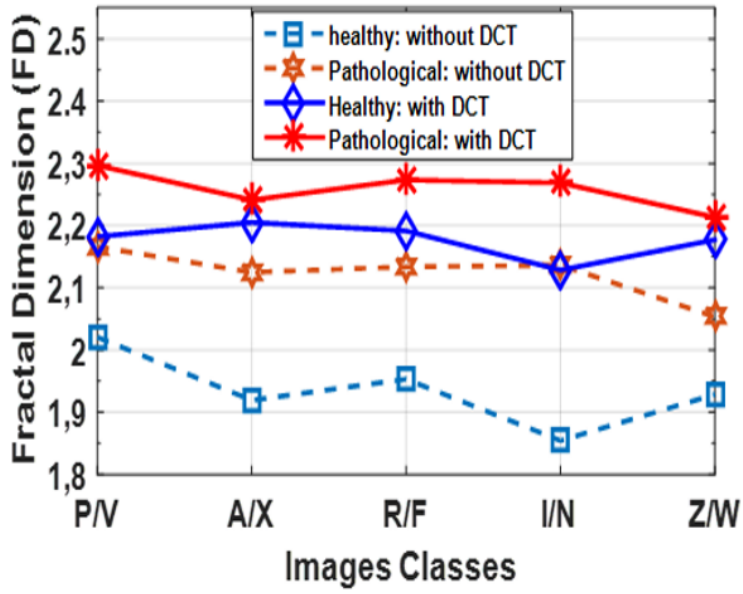

Fig. 9 Variation of the *FD* preprocessed using CE with DCT 50% and without DCT for X-Ray images.

Figure 10 highlights the range in the variations of the fractal dimension values for various DCT percentages (DCT%) in the case of CE-preprocessing applied to MRI texture images, discriminating Healthy and Osteoporosis cases.

Figure 11(Figure 12) exhibits the overall performance of CE preprocessed MRI (X-Ray) texture images in terms of *FD* range values over three distinct classes: non-noisy images without DCT features, non-noisy images with 25% DCT, noisy images with 25% DCT.

From these figures, one notices the absence of overlapping in the *FD* range estimates on non-noisy images preprocessed using the CE method with 25% DCT, which testifies of the ability of the developed *FD*-based approach to discriminate healthy and osteoporosis cases. Although, the use of CE in MRI (X-Ray) texture images showed successful discrimination even in the case of noisy-images. In contrast, the use of CE or MF without DCT indicates an overlap between the healthy cases and the osteoporosis cases, and therefore, we cannot distinguish healthy trabecular textures from the osteoporosis cases in the spatial domain using DBCM.

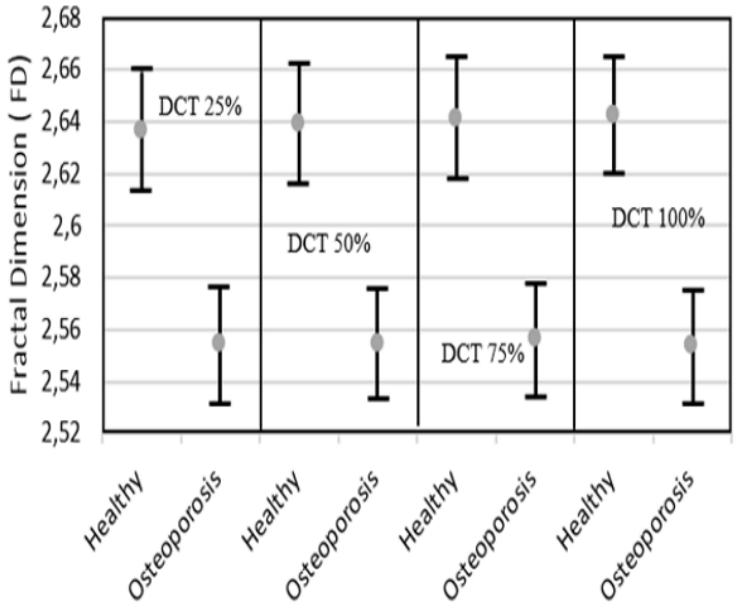

Fig. 10 *FD* results using DBCM with preprocessing (CE) for different DCT percentages (CE+DCT%) for MRI.

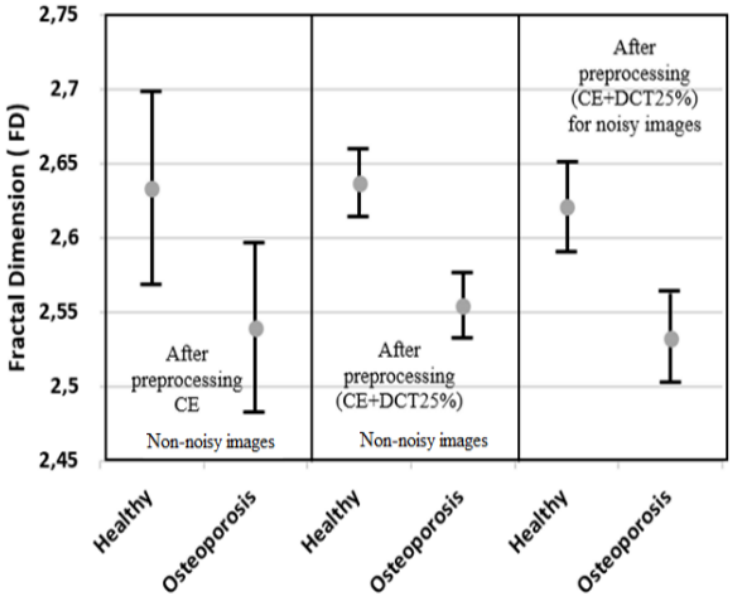

Fig. 11 *FD* results using DBCM with (Contrast Enhancement (CE), (CE+ DCT25%)) for MRI.

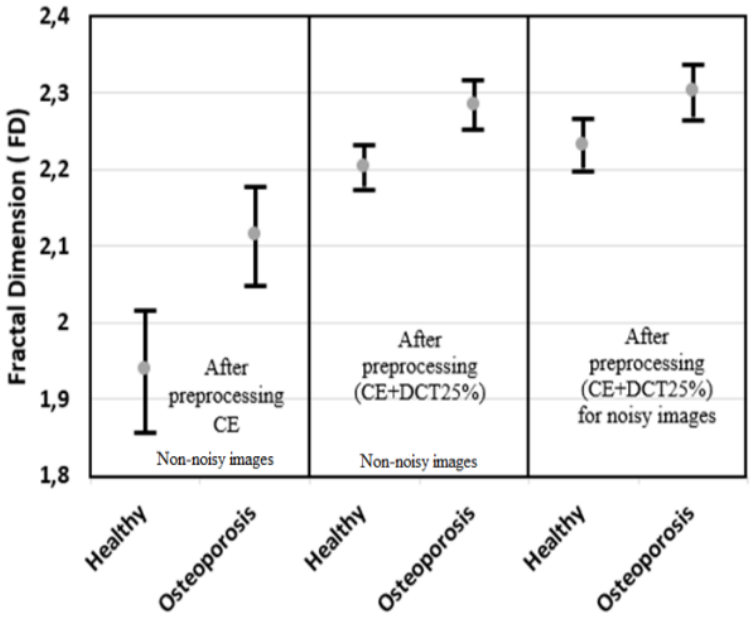

Fig. 12 *FD* results using DBCM with ((CE), (CE+ DCT25%)) for X-Ray images.

4.4 *Directional analysis (anisotropic analysis)*

According to the anisotropic property of the trabecular texture, different characteristics can be presented for different orientations or directions. To test the developed approach to directional changes, we designed a new experiment in which the original texture images are rotated with incremental angles from 0° to 360° with a step angle of 15° and repeated the *FD* calculus process using both preprocessed and non-preprocessed MRI / X-Ray images. In other words, for each rotated texture, we have applied the DCT followed by the DBCM to the transformed texture to estimate the value of the directional *FD* with the variation of the box sizes from (5: 5: 30) pixels. A total of 25 rotation angles (0°:15°:360°) were generated, yielding 25 different *FD* values for the same texture. Next, these *FD* are averaged across the various angles. This process is applied to both (raw and preprocessed) healthy and osteoporosis texture issues of MRI and X-Ray images. Noisy cases were also created and tested accordingly to quantify the robustness of the approach. Tables 11 and 12 summarize the mean statistical results of directional *FD* for MRI and X-Ray texture images, respectively, using DBCM. For each class, we provide the result in terms of the mean, the standard deviation, the maximum and the minimum of the directional *FD* and the degree of anisotropy (*DA*), which is defined as the ratio between the maximum and the minimum of directional *FD* estimate (equation (2)). The associated $p - value$ for both MRI and X-Ray images are also reported.

$$DA = \frac{\max(FD)}{\min(FD)} \tag{2}$$

Table 11 Statistical analysis of directional *FD* using preprocessing (CE or MF)+rotations (0°:15°:360°)+ DCT+DBCM for MRI.

Preprocessing	Cases	$m \pm \sigma$	max	min	DA	$p-value$
Without Preproc.	Healthy	2.6293±0.0653	2.6442	2.5774	1.0259	0.0831
	Osteoporosis	2.6273±0.0872	2.6424	2.5772	1.0252	
MF	Healthy	2.5875±0.0636	2.5998	2.5491	1.0198	0.0634
	Osteoporosis	2.6357±0.0782	2.6490	2.5963	1.0202	
CE	Healthy	2.6448±0.0821	2.6685	2.4594	1.0850	0.0634
	Osteoporosis	2.6125±0.0716	2.6309	2.5400	1.0357	
(MF)+DCT	Healthy	2.1190±0.0619	2.4026	1.8806	1.2775	4.5482e-4
	Osteoporosis	2.2974±0.0526	2.5807	2.1013	1.2281	
(CE)+DCT	Healthy	2.2016±0.0428	2.4765	1.9798	1.2508	4.1708e-4
	Osteoporosis	2.3730±0.0449	2.6565	2.1781	1.2196	
(CE+DCT) for noisy images	Healthy	2.1943± 0.0627	2.4713	1.9772	1.2498	5.8639e-4
	Osteoporosis	2.3688 ±0.0528	2.6534	2.1629	1.2267	
(MF+DCT) for noisy images	Healthy	2.1430±0.0468	2.4180	1.9362	1.2488	3.7952e-3
	Osteoporosis	2.2953±0.0561	2.5775	2.0964	1.2294	

Table 12 Statistical analysis of directional *FD* using preprocessing (CE or MF)+rotations (0°:15°:360°)+ DCT+DBCM for X-Ray images.

Preprocessing	Cases	$m \pm \sigma$	max	min	DA	$p-value$
Without preproc.	Healthy	2.1672±0.0532	2.1789	2.1429	1.0167	0.0679
	Osteoporosis	2.1963±0.0618	2.2080	2.1644	1.0201	
MF	Healthy	2.1614±0.0578	2.1743	2.1365	1.0176	0.0679
	Osteoporosis	2.1956±0.0630	2.2075	2.1619	1.0210	
CE	Healthy	2.1818±0.0427	2.2060	2.1145	1.0432	0.0634
	Osteoporosis	2.2455±0.0622	2.2646	2.2027	1.0281	
(MF+DCT)	Healthy	2.0282±0.0664	2.3306	1.8472	1.2616	4.7805e-4
	Osteoporosis	2.1977±0.0568	2.5113	2.0054	1.2522	
(CE+DCT)	Healthy	2.0078±0.0396	2.3005	1.8372	1.2521	4.7820e-4
	Osteoporosis	2.1978±0.0422	2.5036	2.0187	1.2402	
(MF+DCT) for noisy images	Healthy	2.0263±0.0661	2.3276	1.8466	1.2604	3.7952e-3
	Osteoporosis	2.1425±0.0575	2.4570	1.9568	1.2556	
(CE+DCT) for noisy images	Healthy	2.0361 ±0.0621	2.3415	1.8441	1.2697	4.8368e-4
	Osteoporosis	2.1801±0.0544	2.4967	1.9985	1.2492	

Figures 13-19 display the mean results of the directional *FD* estimates as a function of angles from 0° to 360° in Polar and Cartesian representation for each case presented in Table 11 and Table 12, where the lines in blue represent the healthy case and the lines in red represent the osteoporosis case. A quick look at these figures shows important variations in the *FD* estimates with respect to rotational angles, especially in the Cartesian frame, which, somehow demonstrates the anisotropy property of the trabecular textures. Figures 20 and 21 highlight the overall average of the means of directional *FD* estimates of each class for MRI. More specifically, Figure 20 uses the median filter as preprocessing applied to MR images, while Figure 21 uses the contrast enhancement as a preprocessing method applied to X-Ray images. From these two figures, one notices that there is no overlapping using (CE+DCT), and, thereby, we can classify the healthy trabecular textures from the osteoporosis cases in the DCT domain using DBCM. In contrast, the use of CE or MF without DCT indicates an overlap between the healthy cases and the osteoporosis cases, and therefore, we cannot classify the healthy trabecular texture from the osteoporosis cases in the spatial domain using DBCM.

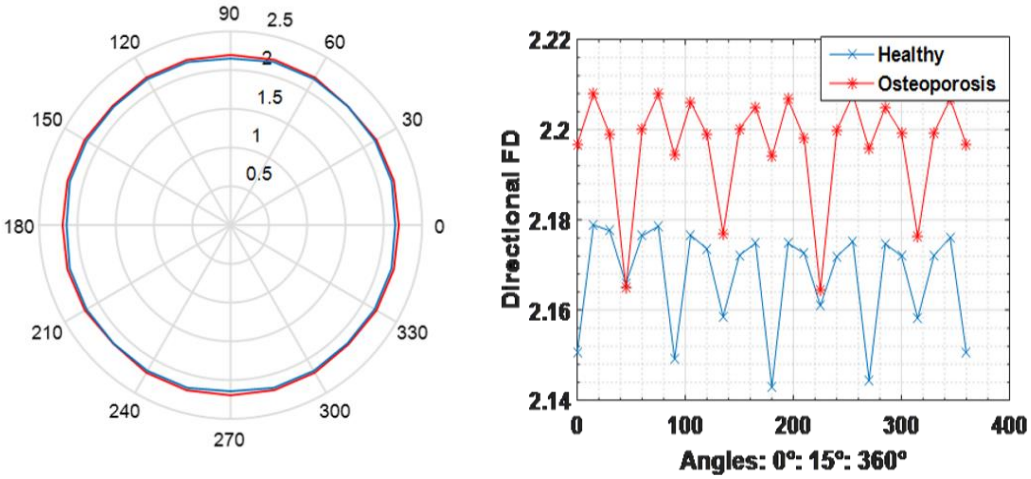

Fig. 13 Results of directional *FD* without preprocessing for X-Ray images in polar and Cartesian representation.

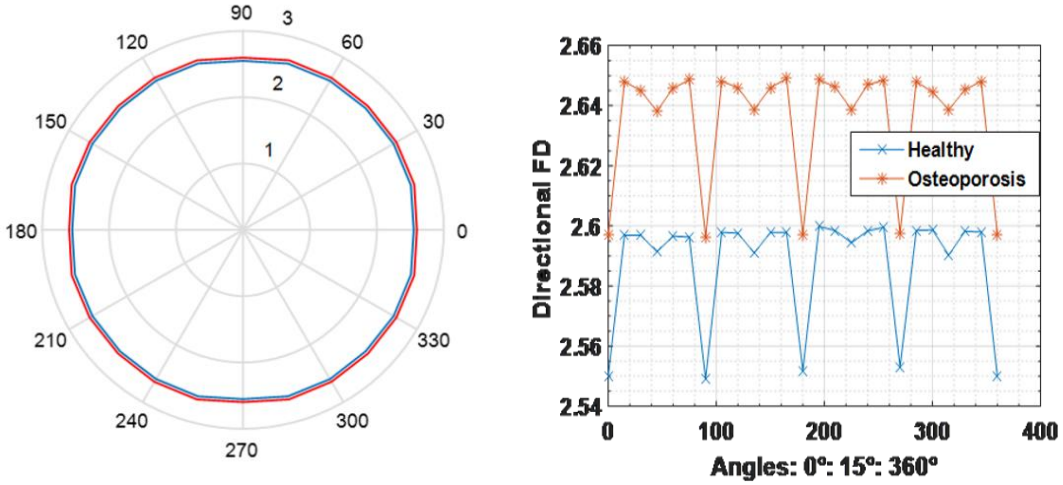

Fig. 14 Results of directional *FD* with preprocessing MF for MRI in polar and Cartesian representation.

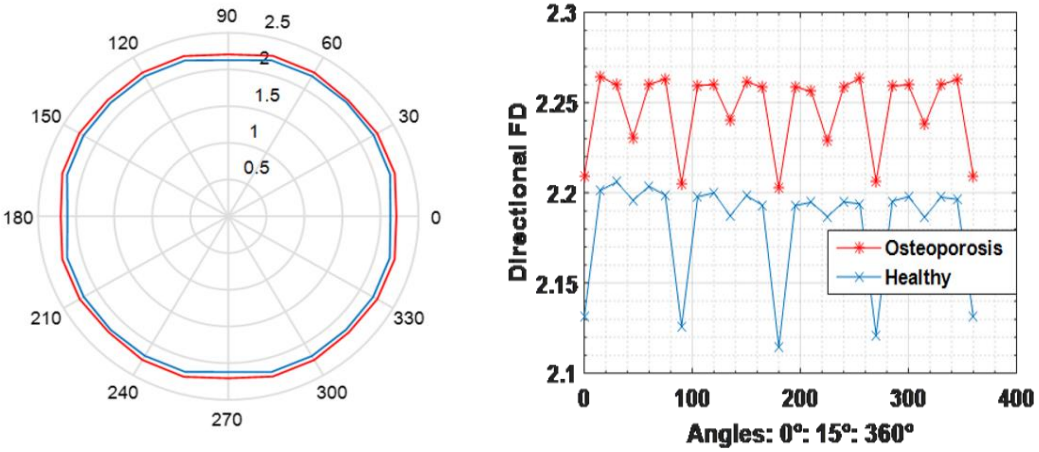

Fig. 15 Results of directional *FD* with preprocessing CE for X-Ray images in polar and Cartesian representation.

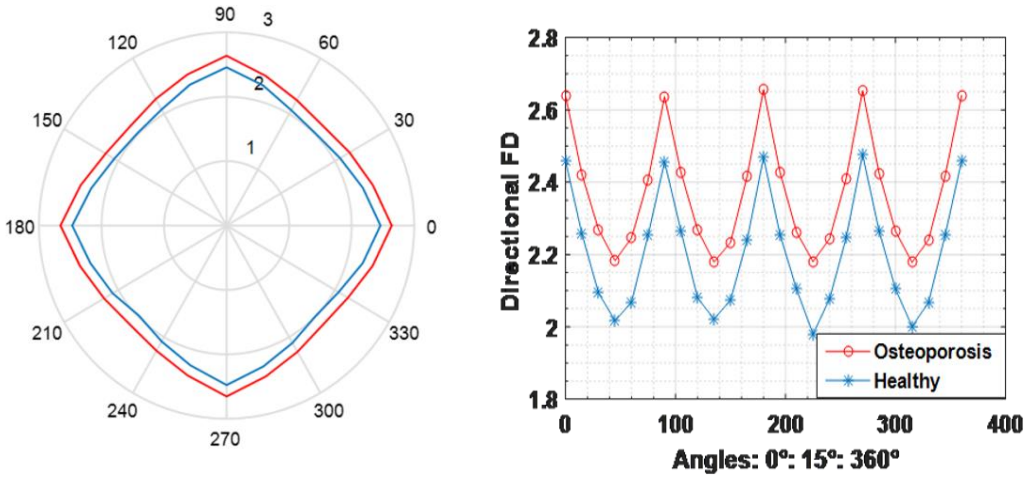

Fig. 16 Results of directional DBCM in the DCT domain using preprocessing (CE) for MRI in polar and Cartesian representation.

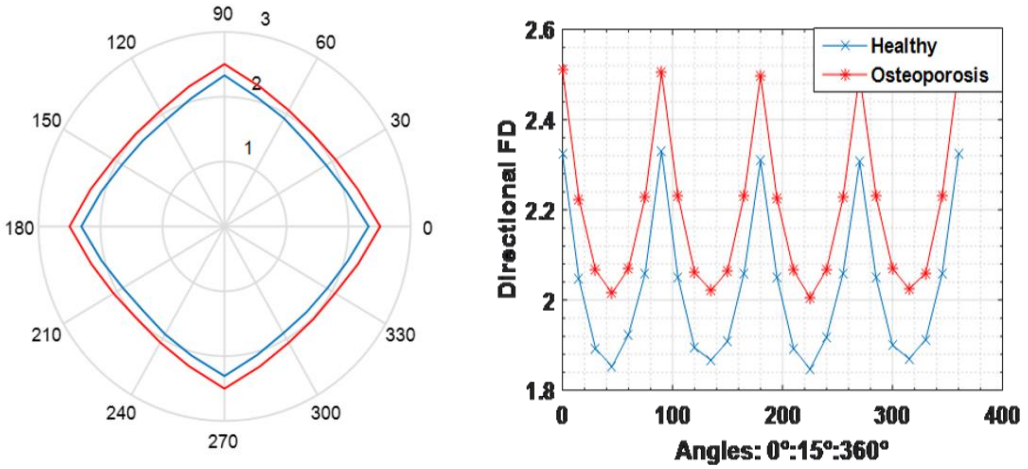

Fig. 17 Results of directional DBCM in the DCT domain using preprocessing (MF) for X-Ray images in polar and Cartesian representation.

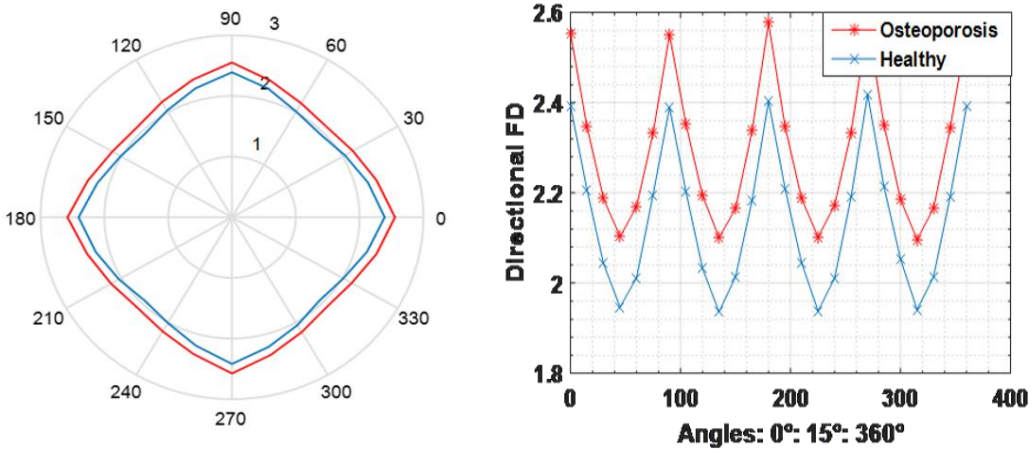

Fig. 18 Results of directional DBCM in the DCT domain using preprocessing (MF) for noisy MRI in polar and Cartesian representation.

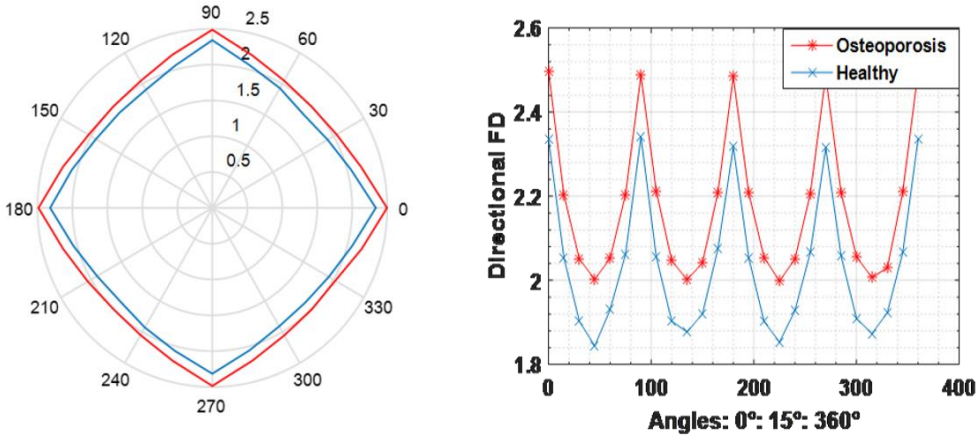

Fig. 19 Results of directional DBCM in the DCT domain using preprocessing (CE) for noisy X-Ray images in polar and Cartesian representation.

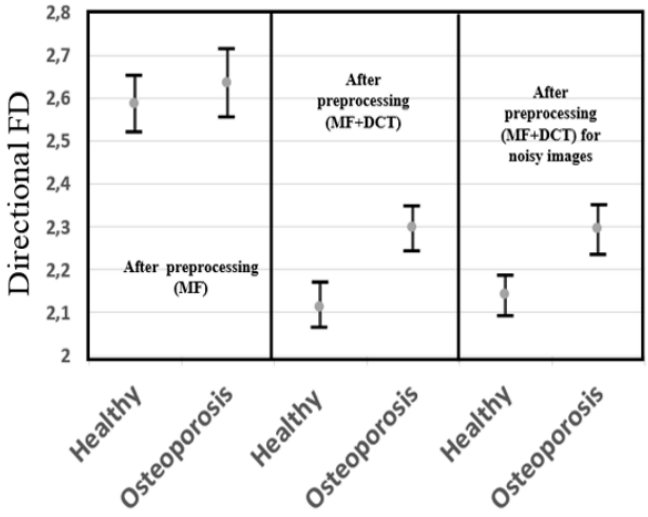

Fig. 20 Mean directional *FD* results using DBCM with preprocessing median filter in DCT domain for MRI.

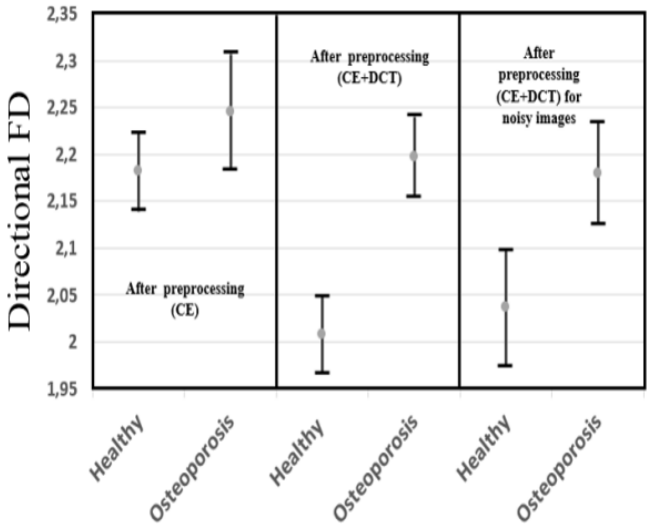

Fig. 21 Mean directional *FD* results using DBCM with preprocessing contrast enhancement (CE) in DCT domain for X-Ray images.

4.5 *Robustness to noise*

Given the various sources of uncertainty pervading the image acquisition process including both operator expertise and general environmental conditions that could substantially undermine the quality of the underlying images, which in turn might affect the subsequent diagnosis, we selected a random sample of noisy images (of low to medium noise intensity) in order to test the robustness of the developed approach. The images were generated by injecting a random noise of low to medium intensity into real images for both MRI and X-Ray imaging modalities, starting from an additive noise of zero mean and standard deviation of 0.01 as pointed out in subsection 3.3. The results of *FD* estimation are summarized in Figures 11, 12, 20 and 21. The latter exhibits the range of *FD* values for both healthy and osteoporosis cases with comparison to non-noisy images distinguishing the cases of the presence and absence of DCT processing. Especially, the absence (resp. presence) of overlapping among the range of *FD* estimates (for healthy and osteoporosis) testifies the success (resp. failure) of the *FD*-based diagnosis operation. The ability of the approach to discriminate healthy and osteoporosis cases demonstrate the robustness of the approach in the presence of disturbances.

A quick look at the results highlighted in Figures 11, 12, 20 and 21 reveals the robustness of the approach for both MRI and X-Ray images. This issue will be discussed in the next subsection.

4.6 *Discussion*

The analysis of the results displayed in the previous subsections reveals the following:

1) The importance of the preprocessing stage cannot be ignored in robustifying the estimation of the fractal dimension[54]. Intuitively, both median filter and contrast enhancement help in dealing with low noise intensity that may occur in the original image database while highlighting key patterns in the images. This, in turn, enhances the *FD* estimation as it can be noticed through a decrease in $p-value$ as compared to Tables 5 and 6 (without preprocessing). On the other hand, in terms of the absolute value of the *FD* estimate, one notices an increase when the median-filter preprocessing stage has been introduced. For instance, this goes from 2.6930 ± 0.1172 to 2.7407 ± 0.0864 for healthy and from 2.6262 ± 0.1094 to 2.6390 ± 0.0817 for osteoporosis cases for MRI images. While a relatively constant *FD* estimate is noticed in case of X-Ray images, e.g., 1.9832 ± 0.1314 to 1.9983 ± 0.0649 for healthy and 2.0999 ± 0.1136 to 2.1531 ± 0.0823 for osteoporosis cases. However, such a trend is not preserved when contrast enhancement preprocessing is applied. One notices a decrease in *FD* value for healthy cases (from 2.6930 ± 0.1172 to 2.6334 ± 0.0649 for MRI, $1.9832\pm0.1314$to $1.9381\pm0.0795$for X-Ray images) and a decrease/increase in *FD* for osteoporosis cases (2.6262 ± 0.1094 to 2.5398 ± 0.0576 for MRI, 2.0999 ± 0.1136 to 2.1153 ± 0.0647 for X-Ray images).
2) The application of the preprocessing stage alone, either median filter or contrast enhancement, is proven not sufficient to ensure a clear distinction between healthy and osteoporosis cases as demonstrated by a $p-value$ greater than 0.05 and a negative Δ.
3) According to Figures 6 and 7 (right), the use of the *PSNR* metric reveals that the median filter yields a better result than contrast enhancement for both MRI and X-Ray images. On the other hand, according to the *SSIM* metric, the graph reveals mixed results where CE outperforms (underperforms) MF in the case of MRIs

dataset (X-Ray dataset).

4) The contribution of the discrete cosine transform (DCT) is clearly noticed from Tables 8-10 and Figures 8-12, Tables 11-12 and Figures 16-21 for directional analysis. Indeed, regardless of whether the median filter or contrast enhancement preprocessing has been employed, the application of DCT systematically leads to a clear distinction between healthy and osteoporosis patterns as demonstrated by positive values of Δ and $p - value$ ($p \leq 0.05$), regardless the percentage of DCT coefficients employed. This result is valid for both MRI and X-Ray images of the database. Besides, monitoring individual values of *FD* for individual images over the 10 key image types in the database shows no occurrence of overlapping when DCT has been employed. Besides, through monitoring the mean values of *FD* estimate for each class (healthy and osteoporosis) presented in Figures 13-21, no occurrence of overlapping when DCT has been employed even in the presence of noise was shown.
5) From figures 14 to 19, we note that the variation of the directional *FD* shape from 0° to 90° is repeated three times from 90° to 180°, from 180° to 270° and from 270° to 360°.
6) Through monitoring the *FD* value, one notices that the fractal dimension increases systematically when DCT was employed as a counterpart to its value when DCT is ignored. This applies to both MRI and X-Ray images regardless of whether the median filter or contrast enhancement was employed.
7) Overall comparison between the median filter and contrast enhancement as preprocessing stages for discrete cosine transform reveals mixed results, where according to Δ values, a clear superiority of the median filter is noticed in case of MRI images and contrast enhancement in case of X-Ray images. Intuitively this is also explained by the lower quality of X-Ray images of the database, which requires contrast enhancement to highlight key patterns of the images.
8) Comparing the results with various percentages of DCT coefficients reveals that *FD* exhibits a roughly constant value (the change occurs only up to a third decimal number) regardless of whether a median filter or contrast enhancement has been employed. This demonstrates that the use of a small percentage (25% for both MRI and X-Ray images) is enough to guarantee a clear distinction between healthy and osteoporosis cases. Figure 10 presents an example of results with preprocessing contrast enhancement (CE) with different DCT percentages (CE+DCT%) in the case of MRI.
9) The results highlighted in subsection 4.2 indicated that *FD* estimated by linear regression through the DCBM method is sensitive to the interval of scales considered during the operation of box-counting. It also shows that DBCM is very sensitive to the presence of important grey-level variations at relatively isolated locations (e.g., presence of singularity)[55]. Therefore, the use of DCT is shown to robustify the *FD* estimation by making the estimate less sensitive to such phenomena (box sizes, singularities). This is due to both the denoising ability introduced by the preprocessing stage and the frequency handling conveyed by the DCT-based approach.
10) The directional fractal analysis reinforces the property of the anisotropy of the trabecular bone textures, and we still can separate the healthy cases from the non-

healthy ones in both MRI and X-Ray imaging modalities using the mean directional *FD* estimate for each class, or the degree of anisotropy, *DA*, for each class, where the results indicate $p-values$ $(p < 0.0004)$.

11) Strictly speaking, as already pointed out in the introduction part of this paper, the DCT is widely applied in the field of image compression, and up to some extent to image classification. To our knowledge, the DCT has not been previously applied to fractal analysis for texture characterization of trabecular bone texture.
12) Comparing our results with alternative results in[51] where the same image database has been employed (X-Ray images) and an alternative method based on variational and morphological cover reveals a mean *FD* of 2.91±0.15 for healthy cases and 2.72±0.15 for osteoporosis, which constitutes a slight increase compared to *FD* results obtained in our study. Besides a more noticeable distinction between healthy and osteoporosis cases is observed in our study.
13) Comparing our results with alternative results in[35] and [38], where the authors used the X-Ray trabecular textures of calcalneus, although the database is very different, the trabecular textures have the same properties. The authors used the directional fractal analysis and estimated the Hurst parameter (H_{mean}) with different estimators. Besides, due to the analogy between Hurst parameter and fractal dimension, equivalent results in terms of the ability of *FD* estimate to differentiate healthy from non-healthy cases can be derived accordingly.
14) Although the process of noising original images by injecting random noise uniformly distributed in the image region, which is commonly employed in the image processing community, can be debatable, the results of subsection 4.5 evaluate the robustness of the developed approach. The marginal failure to fully discriminate osteoporosis cases in X-Ray images is mainly rooted back to the quality of the X-Ray images themselves as already pointed out.
15) The preceding demonstrates the simplicity and computational attractiveness of the developed approach whose algorithmic complexity is of the order of $\frac{N}{8}\log_2\frac{N}{8}$ where N stands for the size of the image, which, in turn, likely yields important gain in terms of medication cost. The accuracy[56] of the developed approach to characterize the trabecular bone texture is exemplified through a $p-value$ $(p < 0.0001)$. It is a pragmatic and clinically effective method, which has been implemented on a prototype device where the first validation tests were promising.
16) The results reported in this study correspond to a single configuration of the acquisition devices (X-Ray and MRI devices). However, a growing number of studies reported the impact of the acquisition parameters on the quality of the image outputted by the MRI or X-Ray devices, which can potentially influence the FD estimate as well. Unfortunately, while acknowledging the importance of such factors, we do not have access directly to the measurement devices in order to tune the acquisition parameters, and test subsequent hypotheses. Therefore, we cannot speculate on the potential impact of such factors on the FD estimates of our developed approach. Intuitively, one may guess that some adjustments that

will be brought by the change in acquisition parameters can be compensated by the preprocessing stage and thereby leaves the FD estimates unchanged. However, other adjustments can induce stronger changes in the morphology of the output image, which cannot be compensated by the preprocessing stage, and, thereby, expects a non-negligible impact on the FD estimates.

5 Conclusion

In this paper, a new method for a robust estimation of the fractal dimension for trabecular bone texture analysis is put forward. The approach builds on a fruitful combination of DCT coefficients and the differential box-counting method (DBCM) while contrasting two commonly employed preprocessing techniques: median filter and contrast enhancement. Such an approach is found very useful to handle the sensitivity of the standard DBCM approach to both box-size variations and the presence of singularities. The developed methodology was applied to a large database of trabecular bone texture containing both MRI and X-Ray images of healthy and osteoporosis tissues. The algorithm is shown to be simple, effective and computationally attractive to characterize the trabecular bone texture. The approach has demonstrated a successful separation of osteoporosis and healthy cases as highlighted by both statistical analyses, through the Wilcoxon rank-sum test, using $p - value$ and overall margin difference, and the monitoring of individual FD values of separate images. The results also show a steady-state of the FD estimate for the various proportion of DCT coefficients employed, which demonstrates that the objective of distinguishing healthy patterns from osteoporosis cases can be achieved with only a minimum level of DCT percentage, where a quarter of DCT coefficients suffices to characterize osteoporosis tissues. The proposed approach is pragmatic and clinically effective, which can be implemented on a prototype device where the first validation tests are promising. The results exhibited in this paper open new challenges to estimating the fractal dimension, which rather focuses on image transforms instead of complex transformations of the differential box-counting method that have been pursued by some scholars. From a medical diagnosis perspective, our results suggest that bone texture analysis might be a useful tool in the assessment of osteoporosis. On the other hand, in the light of alternative studies, one may also expect that through monitoring the evolution of the FD estimate, one may gain further insights into the mechanisms of tumor growth.

As a way forward, the work opens new perspectives for enhancing the FD estimation-based approach by introducing new features as a result of a fruitful combination of basic processing stages with a frequency[57] like transforms to test the ability of fractal dimension to distinguish healthy and non-healthy tissues using a variety of medical imaging datasets.

Disclosures

The authors declared that they have no conflicts of interest.

Acknowledgements

the authors wish to thank P. Dubois of INSERM of Lille for providing us with the database.

References

1. S. Femmam, N. K. M'Sirdi and A. Ouahabi, "Perception and characterization of materials using signal processing techniques," *IEEE Transactions on Instrumentation and Measurement*, 50 (5), 1203-1211(2000).
2. M. Nixon and A. S. Aguado, "Feature Extraction and Image Processing for Computer Vision." Academic Press, 3rd Edition, NY, 2012.
3. R. M. Haralick, K. Shanmugam and I. H. Dinstein, "Textural features for image classification," *IEEE Trans. Systems, Man and Cybernetics*, 6 610-621(1973).
4. B. B. Mandelbrot, "The fractal geometry of nature." W.H. Freeman & Company, NY, 1983.
5. K. Falconer, "Fractal geometry: mathematical foundations and applications." John Wiley & Sons, NY, 2004.
6. S. S. Chen, J. M. Keller, and R. M. Crownover, "On the calculation of fractal features from images," *IEEE Trans. Pattern Analysis and Machine Intelligence*,15(10) 1087-1090(1993).
7. W-Y. Hsu, C-C. Lin, M-S. Ju and Y-N. Sun, "Wavelet-based fractal features with active segment selection: Application to single-trial EEG data," *Journal of Neuroscience Methods*, 163(1) 145-160(2007).
8. D-R. Chen, R.-F. Chang, C.-J. Chen, M.-F. Ho, S.-J. Kuo, S.-T. Chen, S.-J. Hung and W. K. Moon, "Classification of breast ultrasound images using fractal feature," *Journal of Clinical Imaging*, 29(4) 235-245(2005).
9. A. Ouahabi and S. Femmam, "Wavelet-based multifractal analysis of 1-D and 2-D signals: new results," *Analog Integrated Circuits and Signal processing*, 69(1) 3-15(2011).
10. M. G. Roberts, J. Grahman and H. Devlin. "Image Texture in dental Panoramic Radiographs as a Potential Biomarker of Osteoporosis," *IEEE Trans. on Biomedical Engineering, 60(9) 2384-2392(2013).*
11. A. Ouahabi, "Signal and image multiresolution analysis." ISTE-Wiley, London, 2012.
12. M. Djeddi, A. Ouahabi, H. Batatia, A. Basarab and D. Kouame, "Discrete wavelet transform for multifractal texture classification: Application to ultrasound imaging," *Proc. of the 17th IEEE International Conference on Image Processing (ICIP) (2010)* Hong Kong, 637-640.
13. O. S. Al-Kadi and D. Watson, "Texture Analysis of Aggressive and Nonaggressive Lung Tumor CE CT Images," *IEEE Trans. on Biomedical Engineering*, 55(7) 1822-1830(2008).
14. A. Ouahabi, "A review of wavelet denoising in medical imaging," *Proc. International Workshop on Systems, Signal Processing and their Applications (IEEE/WoSSPA)* (2013), Algiers, Algeria, 19-26.
15. A. Ouahabi, "Multifractal analysis for texture characterization: A new approach based on DWT," *Proceedings of the 10th International Conference on Information Science, Signal Processing and their Applications (IEEE/ISSPA),* (2010) Kuala Lumpur Malaysia 698-703.
16. D. Ait Aouit and A. Ouahabi, "Nonlinear Fracture Signal Analysis Using Multifractal Approach Combined with Wavelet," *Fractals- Complex Geometry, Patterns, and Scaling in Nature and Society* 19 (18) 175-183(2011).
17. K. R. Rao and P. Yip, "Discrete Cosine Transform: Algorithms, Advantages, Application." Elsevier Science, 2014.

18. P. Telagarapu, V. Jagan Naveen, A. Lakshmi. Prasanthi and G. Vijaya Santhi, "Image Compression using DCT and Wavelet Transformations," *International Journal of Signal Processing, Image Processing and Pattern Recognition*, 4(3) 61-74(2011).
19. J. Choi, Y-S. Chung, K-H. Kim and J-H. Yoo, "Face recognition using energy probability in DCT domain," *Proc. IEEE International Conference on Multimedia and Expo (ICME)*, (2006), Toronto, Canada, 1549-1552.
20. O. Malcai, O., D. A. Lidar, O. Biham, and D. Avnir, "Scaling range and cutoffs in empirical fractals," *Phys. Rev. E* , 56(3) 2817-2828(1997).
21. J. M. Halley, S. Hartley, A. S. Kallimanis, W. E. Kunin, , J. J. Lennon, and S. P. Sgardelis, "Uses and abuses of fractal methodology in ecology," *Ecology Letters* , 7(3) 254-271(2004).
22. Marcin Molski and Jerzy Konarski, "Tumor growth in the space–time with temporal fractal dimension," Chaos Solitons & Fractals 36(4) 811-818(2008).
23. P. Hall, and A. Wood, "On the performance of box counting estimators of fractal dimension," *Biometrika* 80(1) 246-251(1993).
24. A. G. Constantine, and P. Hall, "Characterizing surface smoothness via estimation of effective fractal dimension", *J. Roy. Statist. Soc*. Ser. B 56(1) 97-113(1994).
25. J. T. Kent, and A. T. A. Wood, "Estimating the fractal dimension of a locally self-similar Gaussian process by using increments," *J. Roy. Statist*. Soc. Ser. B 679-699(1997).
26. A. Feuerverger, P. Hall, and A. T. T. Wood, "Estimation of fractal index and fractal dimension of a Gaussian process by counting the number of level crossings," *J. Time Ser. Anal*. 15(6) 587-606(1994).
27. R. Lopes and N. Betrouni, "Fractal and multifractal analysis: a review," *Medical Image Analysis*, 13(4) 634-649(2009).
28. G. Chan, P. Hall, and D. S. Poskitt, "Periodogram-based estimators of fractal properties," The Annals of Statistics 1684-1711(1995).
29. Q. Cheng, "Selection of multifractal scaling breaks and separation of geochemical and geophysical anomaly," *Earth Sci. – Journal of China University of Geosciences*, 12(1) 54-59(2001).
30. T. Geniting, H. Sevcikova and D. Percival, "Estimators of Fractal Dimension: Assessing the Roughness of Time Series and Spatial Data," *Statistical Science*, 247-277(2012).
31. S. Zehani, A. Ouahabi, M. Oussalah, M. Mimi and A. Taleb-Ahmed, "New and Robust Method for Trabecular Bone Texture Based on Fractal Dimension," *Proc. 42th Annual Conference of IEEE Industrial Electronics (IECON)*, Florence, Italy, 992-997(2016).
32. G. Dougherty and G. M. Henebry, "Fractal signature and lacunarity in the measurement of the texture of trabecular bone in clinical CT images," *Medical Engineering & Physics*, 23(6) 369-380(2001).
33. K. Harrar, L. Hamami, E. Lespessailles and R. Jennane, "Piecewise Whittle estimator for trabecular bone radiograph characterization," *Biomedical Signal Processing and Control*, 8(6) 657-666(2013).
34. K. Zheng and S. Makrogiannis,"Bone Texture Characterization for Osteoporosis Diagnosis using Digital Radiography," Conf. Proc. IEEE Eng. Med. Biol. Soc. 1034-1037(2016).
35. H. Oulhaj, M. Rziza, A. Amine, H. Toumi, R. Jennane, and M. El Hassouni, "Trabecular bone characterization using circular parametric models," *Biomedical Signal Processing and Control*, 33 411-421(2017).

36. A. Singh, M. K. Dutta, R. Jennane and E. Lespessailles, "Classification of trabecular bone structure of osteoporotic patients using machine vision," *Computer in Biology and Medicine*, 91 148-158(2017).
37. R. Su, W. Chen, L. Wei, X. Li, Q. Jin and W. Tao, "Encoded Texture Features to Characterize Bone Radiograph Images," *24th International Conference on Pattern Recognition (ICPR)*, Beijing, China, 3856-3861(2018).
38. K. Harrar, R. Jennane, K. Zaouchi, T. Janvier, H. Toumi and E. Lespessailles, "Oriented fractal analysis for improved bone microarchitecture characterization," *Biomedical Signal Processing and Control*, 39 474-485(2018).
39. L. Houam, A. Hafiane, A. Boukrouche, E. Lespessailles, and R. Jennane, "One dimensional local binary pattern for bone texture characterization," *Pattern Analysis and Applications*, 17(1) 179-193(2014).
40. Z. Zou, J. Yang, V. Megalooikonomou, R. Jennane, E. Cheng, and H. Ling, "Trabecular bone texture classification using wavelet leaders", Medical Imaging 2016: Biomedical Applications in Molecular, Structural, and Functional Imaging (Vol. 9788, p. 97880E). International Society for Optics and Photonics.
41. K. Zheng, R. Jennane, and S. Makrogiannis, "Ensembles of sparse classifiers for osteoporosis characterization in digital radiographs", Medical Imaging 2019: Computer-Aided Diagnosis (Vol. 10950, p. 1095024). International Society for Optics and Photonics.
42. M. R. K. Mookiah, A. Rohrmeier, M. Dieckmeyer, K. Mei, F. K. Kopp, P. B. Noel, J. S. Kirschke, T. Baum and K. Subburaj, "Feasibility of opportunistic osteoporosis screening in routine contrast-enhanced multi detector computed tomography (MDCT) using texture analysis," *Osteoporosis International*, 29(4) 825-835(2018).
43. B. B. Mandelbrot and J. W. Van Ness, "Fractional Brownian Motion, Fractional Noise and Applications," *SIAM Review*, 10(4) 422-437(1968).
44. J. M. H. Du Buf, M. Kardan, and M. Spann, "Texture feature performance for image segmentation," Pattern Recognition, 23(3-4) 291–309(1990).
45. B. Chaudhuriand N. Sarkar. "Texture segmentation using fractal dimension," *IEEE Trans. on Pattern Analysis and Machine Intelligence*, 17(1) 72-77(1995).
46. G. Sorwar and A. Abraham. "DCT based texture classification using soft computing approach,"*Malaysian Journal of Computer Science*, 17(1) 13-23(2004).
47. Z. Pan, A.G. Rust and H. Bolouri, "Image redundancy reduction for neural network classification using discrete cosine transforms," *Proc. IEEE-INNS-ENNS, International Joint Conference on Neural Networks (IJCNN)*, Como, Italy, 3 149-154(2000).
48. C. Sanderson and K. K. Paliwal, "Features for robust face-based identity verification," *Signal Processing*, 83(5) 931-940(2003).
49. M. Khider, A. Taleb-Ahmed, P. Dubois and B. Haddad,"Classification of trabecular bone texture from MRI and CT-Scan images by multiresolution analysis," *Proc. 29th Annual International Conference of the IEEE Engineering in Medicine and Biology Society* (EMBS), Lyon, France, 5589-5592(2007).
50. M. Khider, A. Taleb-Ahmed, and B. Haddad, "Generation of synthetic multifractal realistic surfaces based on natural model and lognormal cascade: Application to MRI classification," *Progress in Pattern Recognition, Image Analysis, Computer Vision, and Applications*, 71-78(2010).
51. A. Taleb-Ahmed, P. Dubois, and E. Duquenoy, "Analysis methods of CT-Scan images for the characterization of the bone texture: First results," *Pattern Recognition Letters*, 24(12) 1971-1982(2003).

52. X. C. Jin, S.H. Ong and Jayasooriah, “A practical method for estimating fractal dimension,” Pattern Recognition Letters, 16(5) 457-464(1995).
53. M. Ferroukhi, A. Ouahabi, M. Attari, Y. Habchi and A. Taleb-Ahmed, “Medical Video Coding Based on 2nd-Generation Wavelets: Performance Evaluation,” *Electronics* , 8(1) 88(2019).
54. J. M. Girault, D. Kouame and A. Ouahabi, “Analytical formulation of the fractal dimension of filtered stochastic signal,” *Signal Processing*, 90(9) 2690-2697(2010).
55. T. C. Halsey, M. H. Jensen, L. P. Kadanoff, I. Procaccia and B. I. Shraiman, “Fractal measures and their singularities: the characterization of strange sets,” *Physical Review A*, 33(2) 1141-1151(1986).
56. C. Guetbi, D. Kouame, A. Ouahabi and J. P. Remineras, “New emboli detection methods,” *International IEEE Ultrasonics Symposium Proceedings*, 1119-1122 (1997).
57. A. Ouahabi, C. Depollier, L. Simon and D. Kouame, "Spectrum estimation from randomly sampled velocity data [LDV]," *IEEE Transactions on Instrumentation and Measurement*, 47 (4), 1005-1012, (1998).